Title

MR-based Attenuation Correction for Brain PET Using 3D Cycle-Consistent Adversarial Network.

Journal

IEEE transactions on radiation and plasma medical sciences, 5(2)

ISSN

2469-7311

Authors

Gong, Kuang
Yang, Jaewon
Larson, Peder EZ
et al.

Publication Date

2021-03-01

DOI

10.1109/trpms.2020.3006844

Peer reviewed

HHS Public Access

Author manuscript

IEEE Trans Radiat Plasma Med Sci. Author manuscript; available in PMC 2022 March 01.

Published in final edited form as:

IEEE Trans Radiat Plasma Med Sci. 2021 March ; 5(2): 185–192. doi:10.1109/trpms.2020.3006844.

MR-based Attenuation Correction for Brain PET Using 3D Cycle-Consistent Adversarial Network

Kuang Gong,
Center for Advanced Medical Computing and Analysis, Gordon Center for Medical Imaging, Massachusetts General Hospital and Harvard Medical School, Boston, MA 02114 USA

Jaewon Yang,
Physics Research Laboratory, Department of Radiology and Biomedical Imaging, University of California, San Francisco, CA 94143 USA

Peder E.Z. Larson,
Department of Radiology and Biomedical Imaging, University of California, San Francisco, CA 94143 USA

Spencer C. Behr,
Department of Radiology and Biomedical Imaging, University of California, San Francisco, CA 94143 USA

Thomas A. Hope,
Department of Radiology and Biomedical Imaging, University of California, San Francisco, CA 94143 USA

Youngho Seo,
Physics Research Laboratory, Department of Radiology and Biomedical Imaging, University of California, San Francisco, CA 94143 USA

Quanzheng Li
Center for Advanced Medical Computing and Analysis, Gordon Center for Medical Imaging, Massachusetts General Hospital and Harvard Medical School, Boston, MA 02114 USA

Abstract

Attenuation correction (AC) is important for the quantitative merits of positron emission tomography (PET). However, attenuation coefficients cannot be derived from magnetic resonance (MR) images directly for PET/MR systems. In this work, we aimed to derive continuous AC maps from Dixon MR images without the requirement of MR and computed tomography (CT) image registration. To achieve this, a 3D generative adversarial network with both discriminative and cycle-consistency loss (Cycle-GAN) was developed. The modified 3D U-net was employed as the structure of the generative networks to generate the pseudo CT/MR images. The 3D patch-based discriminative networks were used to distinguish the generated pseudo CT/MR images from the true CT/MR images. To evaluate its performance, datasets from 32 patients were used in the experiment. The Dixon segmentation and atlas methods provided by the vendor and the

correspondence: kgong@mgh.harvard.edu and li.quanzheng@mgh.harvard.edu.

convolutional neural network (CNN) method which utilized registered MR and CT images were employed as the reference methods. Dice coefficients of the pseudo-CT image and the regional quantification in the reconstructed PET images were compared. Results show that the Cycle-GAN framework can generate better AC compared to the Dixon segmentation and atlas methods, and shows comparable performance compared to the CNN method.

Index Terms—

Positron emission tomography; attenuation correction; generative adversarial network; cycle-consistency

I. Introduction

Positron emission tomography (PET) is a powerful functional imaging modality which can detect molecular-level activity in the tissue through the injection of specific tracers. Attenuation correction (AC) is essential for the accurate estimation of radiotracer distribution in PET. Without AC, there will be underestimation of tracer uptake inside the object, and over-estimation near peripheral regions. Because of MR's excellent soft tissue contrast and the ability to perform functional imaging, along with its complementary roles in motion correction and partial volume correction for PET, PET/MR systems begin to be adopted in clinics. In PET/CT systems, the CT image can be used for AC as the HU unit can be transformed to the attenuation coefficients through a bi-linear transform [1]. However, as the MR signal is not directly related to the photon attenuation coefficients and there is no simple transform that can convert an MR image into the attenuation map, AC for PET/MR still needs further investigations to unleash the quantitative merits of PET. For the past decades, various methods have been proposed to generate pseudo CT images based on MR images, through segmentation [2]–[12], atlas [13]–[21], joint emission and transmission estimation [22]–[26], multi-tissue per pixel-based MR sequence developments [27], [28], and machine learning[29]–[31] approaches.

Due to its strong approximation ability, deep learning has shown promising results for synthetic data generation. As anatomical structures in CT images share similarities with MR images from the same patient, attenuation map generation based on MR images falls into the research category of synthetic data generation. Various methods based on convolutional neural networks (CNNs) have been proposed for pseudo-CT generation, and show better results than state-of-the-art methods for brain [32]–[43], pelvis [44], [45], and whole body [46] regions. All these CNN-based methods train the neural network using existing CT and MR image pairs with the MR images as the input and CT images as the label. However, one problem with the CNN methods is that the MR and CT images need to be paired. It requires a lot of efforts for the image registration process^^ef^^bc^^8c and is difficult for some organs due to non-rigid motions, e.g. lung and abdomen regions. Novel deep learning approaches that can utilize unpaired MR and CT images need further explorations.

Generative adversarial network (GAN) is a framework that contains both generative and discriminative networks, competing with each other to generate new data with the same distribution as the training data [47]–[49]. From the image synthesis point of view, the

generator aims to produce synthetic images that are close to the ground-truth images and the discriminator endeavors to distinguish the synthetic images from the true images. Compared to the explicitly L1- or L2-norm loss widely used in CNN methods, the discriminative loss is data-driven, and the role of the discriminative network is to learn a data-specific training item: the discriminative loss. One advantage of this learned discriminative loss is that the MR and CT images do not need to be paired. For image style transfer, the discriminative loss might be good enough as the overall visual property is important. However, for medical imaging, especially for PET AC, the pixel-to-pixel error between the synthetic image and the ground-truth image is crucial as the local quantitative accuracy is paramount. To stabilize the network training and generate better quantitative results, Dong *et al* [50] combined the pixel-to-pixel difference with the discriminative loss to generate pseudo CT images for brain and pelvis regions. Arabi *et al* [41] included an additional segmentation-based loss to further improve the network performance. However, these approaches still need the paired CT and MR images. Recently the Cycle-GAN method introduces another cycle-consistency loss to stabilize the training process [51] and show better results than using the discriminative loss alone for various applications. It has also been applied to synthetic CT image generation based on 2D networks [52], but not tested for PET AC. A recent work by Dong *et al* [53] proposed a Cycle-GAN framework to learn PET image with AC (PET-AC) from PET image reconstructed with no AC (PET-NAC). Here we focused on predicting pseudo CT image from MR images, and then applying the generated pseudo CT image for PET AC. In this approach, information from PET sinograms, e.g. time-of-flight information, can act as an additional constraint if the generated pseudo CT image is not good enough [54].

In this work, we used clinical brain PET/MR datasets to perform a clinical evaluation of the Cycle-GAN framework for PET AC. As PET data are all acquired in 3D mode clinically, we specifically proposed a 3D Cycle-GAN to fully exploit the axial information. Dixon MR images were employed for pseudo CT generation due to its wide availability in clinical PET/MR scanners. This paper is organized as follows. Section 2 introduces the Cycle-GAN framework and implementation details. Section 3 describes the real data used in the evaluation as well as quantification details. Experimental results are shown in section 4, followed by discussions in section 5. Finally, conclusions are drawn in Section 6.

II. Method

In the Cycle-GAN framework [51], there are four independent networks to train: (1) generative network F, which generates pseudo CT images based on the MR input; (2) generative network B, which generates pseudo MR images based on the CT input; (3) discriminative network D_{CT}, which is used to access whether the generated pseudo CT images are similar to the true CT images or not; (4) discriminative network D_{MR}, which is used to tell whether the generated pseudo MR images are similar to the true MR images or not. Instead of using the L1-norm loss to construct the training function as in CNN methods, the following loss is adopted as the training objective function,

$$L = \sum_{i=1}^{M} \beta_d D_{CT}(F(MR_i), CT_i) + \beta_d D_{MR}(B(CT_i), MR_i) + \beta_c |MR_i - B(F(MR_i))| + \beta_c |CT - F(B(CT_i))|, \quad (1)$$

where the first two items are the discriminative loss and the last two items stand for the cycle-consistency loss. $D_{CT}(F(MR_i), CT_i)$ is used to test whether the generated pseudo CT image $F(MR_i)$, based on the MR input, is similar to the true CT image CT_i. $D_{MR}(B(CT_i), MR_i)$ is used to test whether the generated pseudo MR image $B(CT_i)$, based on the CT input, is similar to the true MR image MR_i. The discriminative loss $D_{CT}(F(MR_i), CT_i)$ and $D_{MR}(B(CT_i), MR_i)$ is constructed based on the least-square loss format as in LSGAN [55]. $|MR_i - B(F(MR_i))|$ is used to ensure that when the pseudo-CT image $F(MR_i)$ is used as the input to generative network B, the output can be similar to the original MR image MR_i. $|CT_i - F(B(CT_i))|$ is used to ensure that when the pseudo MR image $B(CT_i)$ is used as the input to generative network F, the output can be similar to the original CT image CT_i. β_c and β_d are regularization parameters to control the strength of the discriminative loss and the cycle-consistency loss. The whole flowchart of the Cycle-GAN framework is shown in Fig. 1. From the loss function, we can tell that there is no requirement of CT and MR images being registered or even from the same patient. Compared to natural images which are always 2D, the attenuation map used for PET AC is 3D. To better utilize the spatial information along the axial direction, all networks used in our work is 3D network. The generator is based on the 3D Unet structure, where the skip connections can enable better approximation power and the down- and up-sampling layers can reduce the memory requirements. The discriminative network is based on a 3D CNN, which contains several convolutional and down-sampling layers. Details of the generative and the discriminative network structures are shown in Fig. 2. The proposed method is labeled as the Cycle-GAN method in later analysis.

During training and testing, we used 3D patches as the network input due to the GPU memory limit. MR and CT images were scaled to have the same pixel size. The intensity of MR and CT images were scaled to be within the range of 0 to 5 before being used in network training. The patch size is 144 × 144 × 25. Sliding window is set to be 8 along the axial direction to generate the 3D patches. The training batch size was set to 1. The network structures were implemented in Pytorch using Adam algorithm as the optimizer. . 800 epochs were run for the Cycle-GAN method as the training cost function becomes steady after 800 epochs.

III. Experiments

A. Datasets

In total datasets from thirty-two patient (14 males, 18 females, 57.3 ± 10.6 years old [range 29–74]) were included in this study. The study protocol was approved by the local Institutional Review Board (IRB). All patients had whole-body 18F-FDG PET/CT scanning, followed by additional PET/MRI scanning without a second 18F-FDG administration. This study only used the brain data acquired. No pathology in the brain was reported for any of the patients. The average injected dose of 18F-FDG was 307.6 ± 78.8 MBq (range 170.2–

468.1 MBq). Four-fold cross validation was performed to make full use of all the datasets. For each dataset, the CT image was acquired from the GE Discovery PET/CT scanner or the Siemens Biograph HiRez 16 PET/CT scanner. The reconstructed CT image has an axial field of view (FOV) of 700 mm with voxel size 2.73×2.73×3.75 mm^3 if acquired from the GE Discovery PET/CT scanner. It has an axial FOV of 500 mm with voxel size 1.95 × 1.95 × 5.00 mm^3 if acquired from the Siemens Biograph HiRez 16 PET/CT system. The PET/MR datasets were acquired from the GE SIGNA PET/MR system with the transaxial and axial FOV being 600 mm and 250 mm, respectively. The average PET/MR scan duration was 236.1 ± 142.6 s (range 135–900 s). The PET images were reconstructed using the ordered subset expectation maximization (OSEM) algorithm (two iterations with sixteen subsets) with time-of-flight (TOF) information and point-spread-function (PSF) modeling included. The voxel size is 1 × 1 × 2.87 mm^3 and the image size is 300×300×89. Dixon MR images (repetition time, ≈ 4 ms; first echo time/second echo time, 1.3/2.6 ms; flip angle, 5deg; acquisition time, 18 s) were acquired using the head and neck coil array and the image size is 256×256×120 with voxel size 1.93 × 1.93 × 2.6mm^3.

B. Reference methods

Based on the Dixon MR image, water and fat tissues were segmented, and corresponding attenuation coefficients were assigned to generate the attenuation map. This method is denoted as the Segmentation method. The Dixon image can also be registered to the MR template enabled by prior patients' MR and CT pairs through non-rigid registration. Air, soft tissue, sinus and bone can be generated to construct the pseudo CT image [13]. This method is labeled as the Atlas method. We have also added one CNN method [34] based on the U-Net structure as a reference method. The CNN method utilized registered CT and MR images during network training, and the loss function is based on the L1-norm loss between the ground-truth CT and the generated pseudo CT images. Details about the training settings and pre-processing steps of the CNN method are the same as in [34]. For brain PET imaging, the CNN method based on the registered CT and MR images can represent currently the state-of-the-art performance based on supervised learning approaches. Through the comparison with the CNN method, we can better know the potentials and further research directions of the Cycle-GAN approach.

C. Data Analysis

To evaluate the prediction accuracy of the trained network, the relative validation loss based on the generated pseudo CT images was calculated as

$$\text{Relative validation error} = \frac{\left|\text{CT}_{\text{generated}} - \text{CT}_{\text{truth}}\right|}{\left|\text{CT}_{\text{truth}}\right|}, \quad (2)$$

where $\text{CT}_{\text{generated}}$ and CT_{truth} are the generated pseudo and ground-truth CT images, respectively. As bone regions are essential components for AC maps, Dice coefficients were calculated for the bone regions to compare the performance of different methods. As the final goal is to apply the generated pseudo CT images for PET AC, evaluation of the PET error caused by the imperfection of pseudo CT images is important. The relative PET error was used as the evaluation metric and calculated as

$$\text{Relative PET error} = \frac{\left|\text{PET}_{\text{pseudoCT}} - \text{PET}_{\text{CT}}\right|}{\left|\text{PET}_{\text{CT}}\right|}, \quad (3)$$

where $\text{PET}_{\text{pseudoCT}}$ is the PET image using the pseudo CT images for AC, and PET_{CT} is the PET image using the ground-truth CT images for AC. The relative PET error inside the whole brain and specific regions were quantified. The masks for the whole brain region and specific regions were defined as in [34] using the MNI-ICBM 152 nonlinear 2009 [56] and the automated anatomical labeling (AAL) templates [57]. Linear regression was performed to test the similarity between PET_{CT} and PET_{CT}. Based on the whole brain mask, the histograms of the error image inside the global brain mask were calculated to compare the global performance regarding, bias, standard deviation and distribution of the error image. Finally, the mean and standard deviation of the relative PET error across all patients for each of the methods were calculated for all the regions and the whole brain.

IV. Results

Table 1 shows quantitative comparisons of the pseudo CT images generated by different methods, regarding the relative validation loss and Dice coefficients in the bone regions. The CNN method has the lowest validation loss and the highest Dice coefficients for the bone regions. The Cycle-GAN method has a better performance regarding the validation loss and Dice coefficients than the Atlas and Segmentation methods. Compared to the CNN method, the Cycle-GAN method has a similar Dice coefficient of bone regions above the eye, but a worse Dice coefficient of bone regions below the eye. This means that the Cycle-GAN method is good at recovering the cortical bone regions, but still need improvements for bone regions below the eye, e.g., bone regions near the sinuses and the mastoid part of the temporal bone. Fig. 3 shows the generated pseudo CT images along with the ground-truth CT image for one subject. Compared with the Segmentation and the Atlas methods, both the CNN and the Cycle-GAN method can better recover the details for the bone and air regions. Based on the same subject as shown in Fig. 3, Fig. 4 shows the standardized uptake value (SUV) images and the SUV error images between the image generated using the ground-truth CT and the PET images generated using the pseudo CT images. The CNN and Cycle-GAN methods can generate smaller PET errors compared to the Segmentation and the Atlas methods. It can be noted from the sagittal view that the Cycle-GAN method has a larger error than the CNN method near the sinus region.

As for quantitative comparisons from all the PET datasets, Fig. 5 shows the Bland-Altman plots for different methods. The mean values of PET error images for the Segmentation, Atlas, CNN and Cycle-GAN methods were 0.219, 0.035, 0.009 and −0.010, respectively. As for the standard deviation of the PET error images, similar standard deviations were observed for the CNN method (0.128) and the Cycle-GAN method (0.134), which were smaller than the Segmentation method (0.242) and the Atlas method (0.208). Fig. 6 presents boxplots of the relative error values for the whole brain and the four lobes as well as cerebellum, putamen and caudate regions. The Cycle-GAN method can generate smaller errors compared with the Segmentation and the Atlas methods. It also has comparable whole and regional brain quantification compared to the CNN method. For the Cycle-GAN

method, we noticed that there were two outliers which had larger relative errors (4.8% and 5.2%) regarding the whole-brain quantification. We further checked those two cases and found that air regions in the mastoid process were mis-classified as bones, which caused larger PET quantification errors.

V. Discussions

In this work, we have generated pseudo CT images based on the 3D Cycle-GAN framework. Unlike CNN methods, the pixel-to-pixel difference between the ground-truth CT and the generated pseudo CT image is not included in the training function for the Cycle-GAN framework. One advantage of the Cycle-GAN framework compared to the CNN framework is that spatial registration or alignment is not needed, which can relax the registration requirements between CT and MR images and has a potential for cases where registration is difficult. Furthermore, based on the loss function of the Cycle-GAN framework, the CT and MR image can come from different patients, which can make the training much easier as the subject does not need to go through both CT and MR scans. In our study, we have tested the cases where the CT and MR images come from different subjects. However, our generated results are not robust enough as compared to using CT and MR images from the same patient. Our thought is that the number of datasets used in the training is not enough to train a Cycle-GAN where MR and CT images come from different patients. The requirement for the scenarios where MR and CT images come from different subjects, regarding the number of training datasets needed, needs further investigations.

Some pre-processing steps were performed on the CT and MR images. The intensity of the input CT or MR images was normalized to 0 to 5 so that better information flow can be enabled during network training. In addition, CT and MR images were resampled to have the same pixel size. For our datasets, no pathology in the brain was reported for any of the patients. As a result, our current study cannot evaluate the prediction accuracy of the Cycle-GAN method for MR images with abnormal regions. We hypothesize that the performance of the Cycle-GAN method cannot be as good as normal brain datasets when the test brain data has pathologies, if the training data do not contain datasets with pathologies.

Regarding CT prediction, based on the experimental results, we noticed that compared to the CNN method, the Dice coefficient of the bone region below the eye in the Cycle-GAN method is a little lower. Through checking the datasets with larger CT errors, we found that for the Cycle-GAN method one challenging part is bone prediction near the sinuses and the mastoid part of the temporal bone. Further improvements are still needed specifically for these regions. Regarding PET quantification, the overall whole and regional quantification performance of the Cycle-GAN method is comparable to that of the CNN method, as shown in Fig. 5 and Fig. 6. As the pixel-to-pixel difference used in the CNN method is a much strong training constraint compared to the cycle-consistency loss and the discriminative loss, current performance achievement of the Cycle-GAN method demonstrates its feasibility for PET attenuation correction. Considering the great potentials of training without paired data, further investigations of using unpaired data for PET AC is worthwhile and in great need. In the future, we will further modify the network structures and explore novel loss items to improve its performance.

The MR sequence used in this work is Dixon MR image, which has wide availability in clinical PET/MR scanners. The Cycle-GAN method can be applied to other MR sequences as well, e.g., T1-weighted, ultrashort echo-time (UTE) and zero echo-time (ZTE) sequences. The Cycle-GAN method can work better if there are better contrast among bone, air and soft tissues in the MR images. Brain study performed in this work is a feasibility test of the Cycle-GAN method. Our results indicate that it has a comparable performance regarding the brain region quantification. Another application of the Cycle-GAN method is whole-body PET AC, where the registration between CT and MR images is much more difficult, and accordingly the Cycle-GAN method can have a larger impact. Extending the Cycle-GAN method to whole-body PET AC is one of our future research directions.

VI. Conclusion

In this work, we proposed and evaluated a 3D Cycle-GAN method for PET/MR AC, where the MR and CT images do not need to be paired. Evaluations based on 32 brain PET/MR datasets demonstrate that the Cycle-GAN approach can generate better pseudo CT images compared to the segmentation and the atlas methods, and has comparable performance compared to the CNN method regarding whole and regional brain quantification.

Acknowledgements

This work was supported in part by the National Institutes of Health under grant R01 AG052653, R21 AG067422 and research support from GE Healthcare.

References

[1]. Carney JP, Townsend DW, Rappoport V et al., “Method for transforming CT images for attenuation correction in PET/CT imaging,” Medical Physics, vol. 33, no. 4, pp. 976–983, 2006. [PubMed: 16696474]

[2]. Martinez-Möller A, Souvatzoglou M, Delso G et al., “Tissue classification as a potential approach for attenuation correction in whole-body PET/MRI: evaluation with PET/CT data,” Journal of Nuclear Medicine, vol. 50, no. 4, pp. 520–526, 2009. [PubMed: 19289430]

[3]. Keereman V, Fierens Y, Broux T et al., “MRI-based attenuation correction for PET/MRI using ultrashort echo time sequences,” Journal of Nuclear Medicine, vol. 51, no. 5, pp. 812–818, 2010. [PubMed: 20439508]

[4]. Berker Y, Franke J, Salomon A et al., “MRI-based attenuation correction for hybrid PET/MRI systems: a 4-class tissue segmentation technique using a combined ultrashort-echo-time/Dixon MRI sequence,” Journal of Nuclear Medicine, vol. 53, no. 5, pp. 796–804, 2012. [PubMed: 22505568]

[5]. Ladefoged CN, Benoit D, Law I et al., “Region specific optimization of continuous linear attenuation coefficients based on UTE (RESOLUTE): application to PET/MR brain imaging,” Physics in Medicine & Biology, vol. 60, no. 20, p. 8047, 2015. [PubMed: 26422177]

[6]. Sekine T, ter Voert EE, Warnock G et al., “Clinical evaluation of zero-echo-time attenuation correction for brain 18F-FDG PET/MRI: comparison with atlas attenuation correction,” Journal of Nuclear Medicine, vol. 57, no. 12, pp. 1927–1932, 2016. [PubMed: 27339875]

[7]. Leynes AP, Yang J, Shanbhag DD et al., “Hybrid ZTE/Dixon MR-based attenuation correction for quantitative uptake estimation of pelvic lesions in PET/MRI,” Medical Physics, vol. 44, no. 3, pp. 902–913, 2017. [PubMed: 28112410]

[8]. Khalifé M, Fernandez B, Jaubert O et al., “Subject-specific bone attenuation correction for brain PET/MR: can ZTE-MRI substitute CT scan accurately?” Physics in Medicine & Biology, vol. 62, no. 19, p. 7814, 2017. [PubMed: 28837045]

[9]. Yang J, Wiesinger F, Kaushik S et al., “Evaluation of sinus/edge corrected ZTE-based attenuation correction in brain PET/MRI,” Journal of Nuclear Medicine, pp. jnumed–116, 2017.

[10]. Wiesinger F, Bylund M, Yang J et al., “Zero TE-based pseudo-CT image conversion in the head and its application in PET/MR attenuation correction and MR-guided radiation therapy planning,” Magnetic resonance in medicine, vol. 80, no. 4, pp. 1440–1451, 2018. [PubMed: 29457287]

[11]. Delso G, Gillett D, Bashari W et al., “Clinical evaluation of 11 C-Met-Avid pituitary lesions using a ZTE-based AC method,” IEEE Transactions on Radiation and Plasma Medical Sciences, vol. 3, no. 4, pp. 504–508, 2018.

[12]. Lindemann ME, Nensa F, and Quick HH, “Impact of improved attenuation correction on 18F-FDG PET/MR hybrid imaging of the heart,” PloS one, vol. 14, no. 3, 2019.

[13]. Wollenweber S, Ambwani S, Delso G et al., “Evaluation of an atlas-based PET head attenuation correction using PET/CT & MR patient data,” IEEE Transactions on Nuclear Science, vol. 60, no. 5, pp. 3383–3390, 2013.

[14]. Burgos N, Cardoso MJ, Thielemans K et al., “Attenuation correction synthesis for hybrid PET-MR scanners: application to brain studies,” IEEE Transactions on Medical Imaging, vol. 33, no. 12, pp. 2332–2341, 2014. [PubMed: 25055381]

[15]. Izquierdo-Garcia D, Hansen AE, Förster S et al., “An SPM8-based approach for attenuation correction combining segmentation and nonrigid template formation: application to simultaneous PET/MR brain imaging,” Journal of Nuclear Medicine, vol. 55, no. 11, pp. 1825–1830, 2014. [PubMed: 25278515]

[16]. Yang J, Jian Y, Jenkins N et al., “Quantitative evaluation of atlas-based attenuation correction for brain PET in an integrated time-of-flight PET/MR imaging system,” Radiology, p. 161603, 2017a.

[17]. Izquierdo-Garcia D, Eldaief MC, Vangel MG et al., “Intrascanner reproducibility of an SPM-based head MR-based attenuation correction method,” IEEE Transactions on Radiation and Plasma Medical Sciences, vol. 3, no. 3, pp. 327–333, 2018. [PubMed: 32537528]

[18]. Mansur A, Newbould R, Searle GE et al., “PET-MR attenuation correction in dynamic brain pet using [11 C] cimbi-36: a direct comparison with PET-CT,” IEEE Transactions on Radiation and Plasma Medical Sciences, vol. 2, no. 5, pp. 483–489, 2018.

[19]. Sousa JM, Appel L, Engström M et al., “Evaluation of zero-echo-time attenuation correction for integrated PET/MR brain imaging?comparison to head atlas and 68 Ge-transmission-based attenuation correction,” EJNMMI physics, vol. 5, no. 1, pp. 1–15, 2018. [PubMed: 29302810]

[20]. Blanc-Durand P, Khalife M, Sgard B et al., “Attenuation correction using 3d deep convolutional neural network for brain 18F-FDG PET/MR: Comparison with Atlas, ZTE and CT based attenuation correction,” PloS one, vol. 14, no. 10, 2019.

[21]. Okazawa H, Tsujikawa T, Higashino Y et al., “No significant difference found in PET/MRI CBF values reconstructed with CT-atlas-based and ZTE MR attenuation correction,” EJNMMI research, vol. 9, no. 1, pp. 1–9, 2019. [PubMed: 30607651]

[22]. Defrise M, Rezaei A, and Nuyts J, “Time-of-flight PET data determine the attenuation sinogram up to a constant,” Physics in Medicine & Biology, vol. 57, no. 4, p. 885, 2012. [PubMed: 22290428]

[23]. Rezaei A, Defrise M, Bal G et al., “Simultaneous reconstruction of activity and attenuation in time-of-flight PET,” IEEE Transactions on Medical Imaging, vol. 31, no. 12, pp. 2224–2233, 2012. [PubMed: 22899574]

[24]. Li Q, Li H, Kim K et al., “Joint estimation of activity image and attenuation sinogram using time-of-flight positron emission tomography data consistency condition filtering,” Journal of Medical Imaging, vol. 4, no. 2, pp. 023 502–023 502, 2017.

[25]. Mehranian A and Zaidi H, “Joint estimation of activity and attenuation in whole-body TOF PET/MRI using constrained Gaussian mixture models,” IEEE Transactions on Medical Imaging, vol. 34, no. 9, pp. 1808–1821, 2015. [PubMed: 25769148]

[26]. Nuyts J, Rezaei A, and Defrise M, “The validation problem of joint emission/transmission reconstruction from TOF-PET projections,” IEEE Transactions on Radiation and Plasma Medical Sciences, vol. 2, no. 4, pp. 273–278, 2018.

[27]. Cencini M, Tosetti M, and Buonincontri G, “An aristotelian view on MR-based attenuation correction (ARISTOMRAC): combining the four elements,” IEEE Transactions on Radiation and Plasma Medical Sciences, vol. 3, no. 4, pp. 491–497, 2019.

[28]. Han PK, Horng DE, Gong K et al., “MR-based PET attenuation correction using a combined ultrashort echo time/multi-echo Dixon acquisition,” arXiv preprint arXiv:2004.01212, 2020.

[29]. Zaidi H, Diaz-Gomez M, Boudraa A et al., “Fuzzy clustering-based segmented attenuation correction in whole-body PET imaging,” Physics in Medicine & Biology, vol. 47, no. 7, p. 1143, 2002. [PubMed: 11996060]

[30]. Johansson A, Karlsson M, and Nyholm T, “CT substitute derived from MRI sequences with ultrashort echo time,” Medical physics, vol. 38, no. 5, pp. 2708–2714, 2011. [PubMed: 21776807]

[31]. Huynh T, Gao Y, Kang J et al., “Estimating CT image from MRI data using structured random forest and auto-context model,” IEEE Transactions on Medical Imaging, vol. 35, no. 1, pp. 174–183, 2016. [PubMed: 26241970]

[32]. Han X, “MR-based synthetic CT generation using a deep convolutional neural network method,” Medical Physics, vol. 44, no. 4, pp. 1408–1419, 2017. [PubMed: 28192624]

[33]. Liu F, Jang H, Kijowski R et al., “Deep learning MR imaging–based attenuation correction for PET/MR imaging,” Radiology, p. 170700, 2017.

[34]. Gong K, Yang J, Kim K et al., “Attenuation correction for brain pet imaging using deep neural network based on dixon and zte mr images,” Physics in Medicine & Biology, vol. 63, no. 12, p. 125011, 2018. [PubMed: 29790857]

[35]. Hwang D, Kim KY, Kang SK et al., “Improving the accuracy of simultaneously reconstructed activity and attenuation maps using deep learning,” Journal of Nuclear Medicine, vol. 59, no. 10, pp. 1624–1629, 2018. [PubMed: 29449446]

[36]. Jang H, Liu F, Zhao G et al., “Deep learning based mrac using rapid ultrashort echo time imaging,” Medical physics, vol. 45, no. 8, pp. 3697–3704, 2018.

[37]. Ladefoged CN, Marner L, Hindsholm A et al., “Deep learning based attenuation correction of pet/mri in pediatric brain tumor patients: Evaluation in a clinical setting,” Frontiers in neuroscience, vol. 12, p. 1005, 2018.

[38]. Liu F, Jang H, Kijowski R et al., “A deep learning approach for 18 F-FDG PET attenuation correction,” EJNMMI physics, vol. 5, no. 1, pp. 1–15, 2018. [PubMed: 29302810]

[39]. Spuhler KD, Gardus J, Gao Y et al., “Synthesis of patient-specific transmission data for pet attenuation correction for pet/mri neuroimaging using a convolutional neural network,” Journal of Nuclear Medicine, vol. 60, no. 4, pp. 555–560, 2019. [PubMed: 30166355]

[40]. Yang J, Park D, Gullberg GT et al., “Joint correction of attenuation and scatter in image space using deep convolutional neural networks for dedicated brain 18f-fdg pet,” Physics in Medicine & Biology, vol. 64, no. 7, p. 075019, 2019. [PubMed: 30743246]

[41]. Arabi H, Zeng G, Zheng G et al., “Novel adversarial semantic structure deep learning for MRI-guided attenuation correction in brain PET/MRI,” European journal of nuclear medicine and molecular imaging, vol. 46, no. 13, pp. 2746–2759, 2019. [PubMed: 31264170]

[42]. Shiri I, Ghafarian P, Geramifar P et al., “Direct attenuation correction of brain pet images using only emission data via a deep convolutional encoder-decoder (deep-dac),” European radiology, pp. 1–13, 2019.

[43]. Armanious K, K^^c3^^bcstner T, Reimold M et al., “Independent brain F-FDG PET attenuation correction using a deep learning approach with generative adversarial networks,” Hellenic journal of nuclear medicine, vol. 22, no. 3, pp. 179–186, 2019. [PubMed: 31587027]

[44]. Leynes AP, Yang J, Wiesinger F et al., “Direct pseudoct generation for pelvis PET/MRI attenuation correction using deep convolutional neural networks with multi-parametric MRI: Zero echo-time and dixon deep pseudoCT (ZeDD-CT),” Journal of Nuclear Medicine, pp. jnumed–117, 2017b.

[45]. Torrado-Carvajal A, Vera-Olmos J, Izquierdo-Garcia D et al., “Dixon-vibe deep learning (divide) pseudo-ct synthesis for pelvis pet/mr attenuation correction,” Journal of Nuclear Medicine, vol. 60, no. 3, pp. 429–435, 2019. [PubMed: 30166357]

[46]. Hwang D, Kang SK, Kim KY et al., “Generation of pet attenuation map for whole-body time-of-flight 18f-fdg pet/mri using a deep neural network trained with simultaneously reconstructed activity and attenuation maps,” Journal of Nuclear Medicine, pp. jnumed–118, 2019.

[47]. Goodfellow I, Pouget-Abadie J, Mirza M et al., “Generative adversarial nets,” in Advances in neural information processing systems, 2014, pp. 2672–2680.

[48]. Radford A, Metz L, and Chintala S, “Unsupervised representation learning with deep convolutional generative adversarial networks,” arXiv preprint arXiv:1511.06434, 2015.

[49]. Isola P, Zhu J-Y, Zhou T et al., “Image-to-image translation with conditional adversarial networks,” in Proceedings of the IEEE conference on computer vision and pattern recognition, 2017, pp. 1125–1134.

[50]. Nie D, Trullo R, Lian J et al., “Medical image synthesis with context-aware generative adversarial networks,” Proceedings of International Conference on Medical Image Computing and Computer-Assisted Intervention, pp. 417–425, 2017.

[51]. Zhu J-Y, Park T, Isola P et al., “Unpaired image-to-image translation using cycle-consistent adversarial networks,” in Proceedings of the IEEE international conference on computer vision, 2017, pp. 2223–2232.

[52]. Wolterink JM, Dinkla AM, Savenije MH et al., “Deep mr to ct synthesis using unpaired data,” in International Workshop on Simulation and Synthesis in Medical Imaging. Springer, 2017, pp. 14–23.

[53]. Dong X, Lei Y, Wang T et al., “Deep learning-based attenuation correction in the absence of structural information for whole-body PET imaging,” Physics in medicine and biology, vol. 65, no. 5, p. 055011, 2020. [PubMed: 31869826]

[54]. Gong K, Berg E, Cherry SR et al., “Machine learning in PET: From photon detection to quantitative image reconstruction,” Proceedings of the IEEE, vol. 108, no. 1, pp. 51–68, 2019.

[55]. Mao X, Li Q, Xie H et al., “Least squares generative adversarial networks,” in Proceedings of the IEEE International Conference on Computer Vision, 2017, pp. 2794–2802.

[56]. Fonov VS, Evans AC, McKinstry RC et al., “Unbiased nonlinear average age-appropriate brain templates from birth to adulthood,” NeuroImage, vol. 47, p. S102, 2009.

[57]. Holmes CJ, Hoge R, Collins L et al., “Enhancement of MR images using registration for signal averaging,” Journal of Computer Assisted Tomography, vol. 22, no. 2, pp. 324–333, 1998. [PubMed: 9530404]

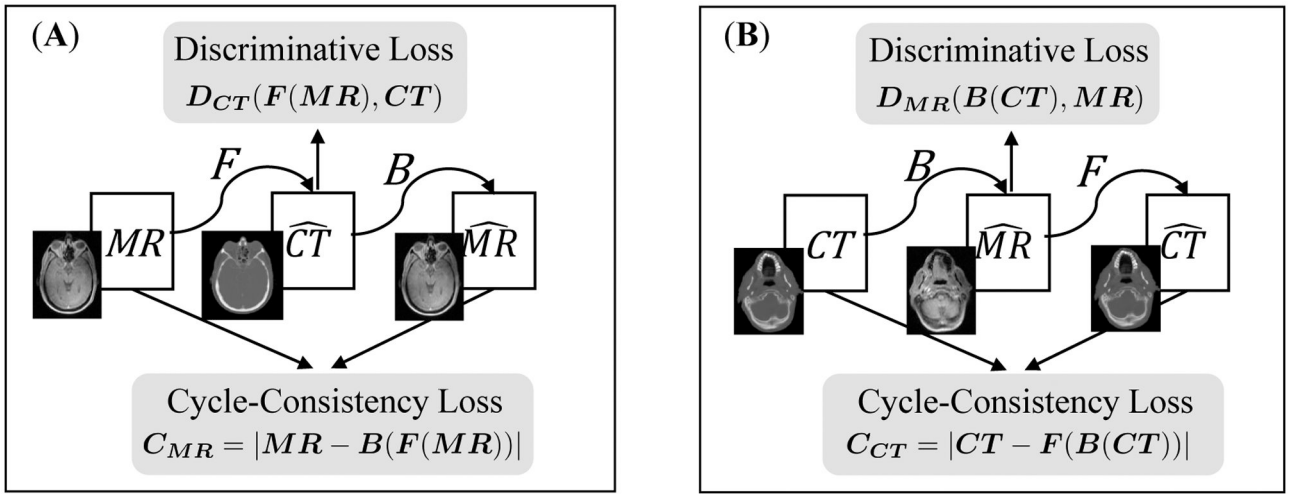

Fig. 1:

The diagram of the Cycle-GAN framework used in this work. It consists of two generators: F and B, and two discriminators: D_{MR} and D_{CT}. (A) the path where the generator input is MR image and the discriminator input are CT and the generated pseudo CT images. (B) the path where the generator input is CT image and the discriminator input are MR and the generated pseudo MR images. Detailed network structures for the generators and the discriminators are shown in Fig. 2.

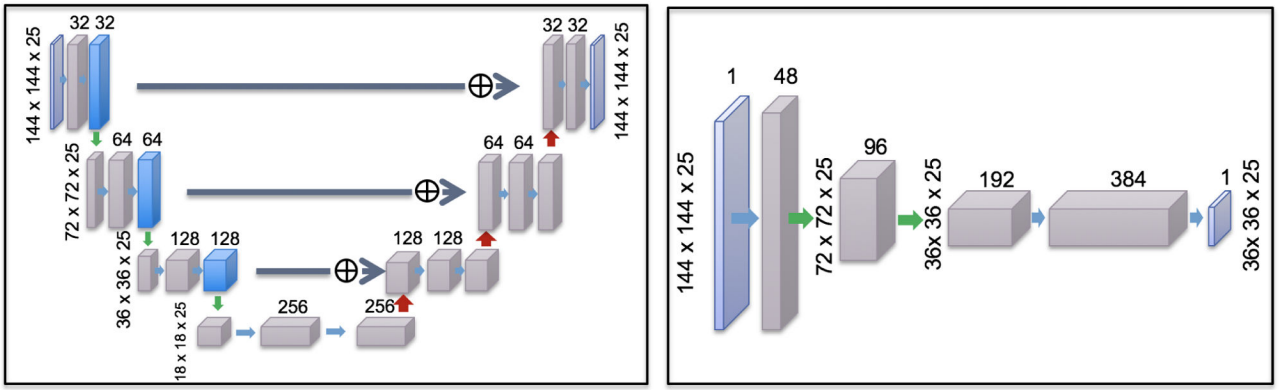

Fig. 2:

The diagrams of network structures used in this work. The left diagram is the 3D U-net structure employed as the generator network. The right diagram is the 3D CNN used for the patch-based discriminator. For both networks, the number on each layer indicates the 3D patch size.

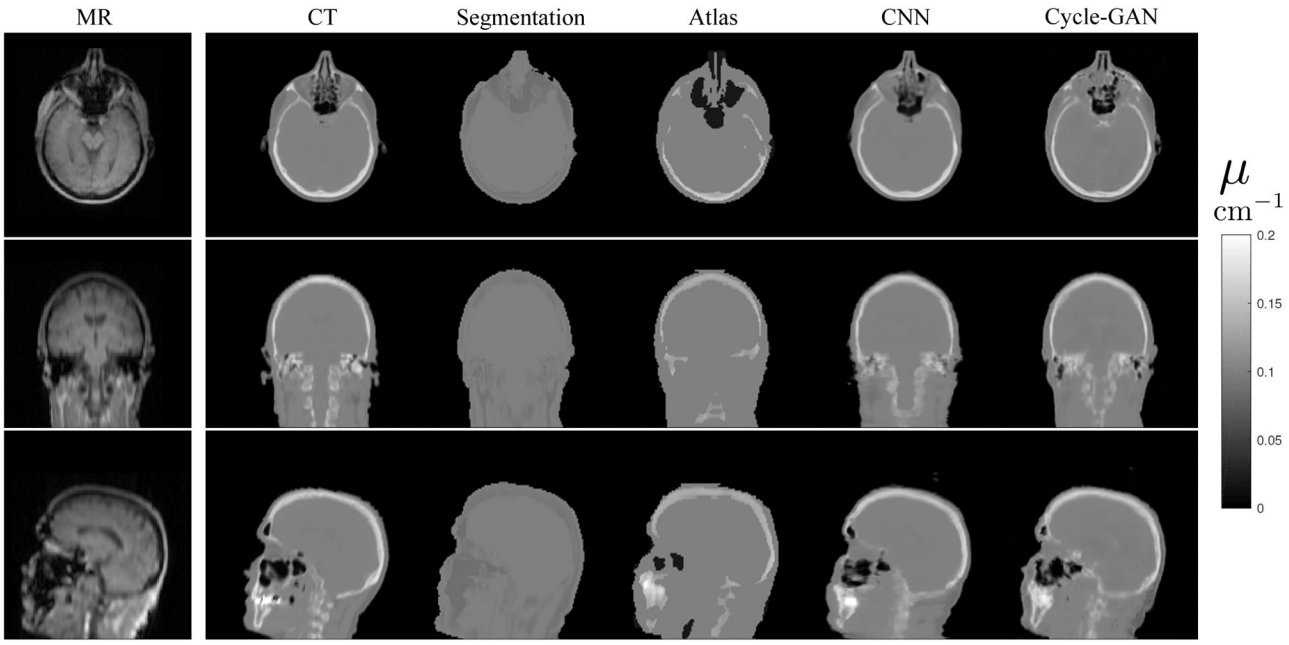

Fig. 3:

Three views of the MR and the attenuation maps based on ground-truth CT and generated pseudo CT images. From left to right, each column represents the MR images, the attenuation map based on ground-truth CT images, and the attenuation maps generated through the Segmentation method, the Atlas method, the CNN method, and the Cycle-GAN method, respectively.

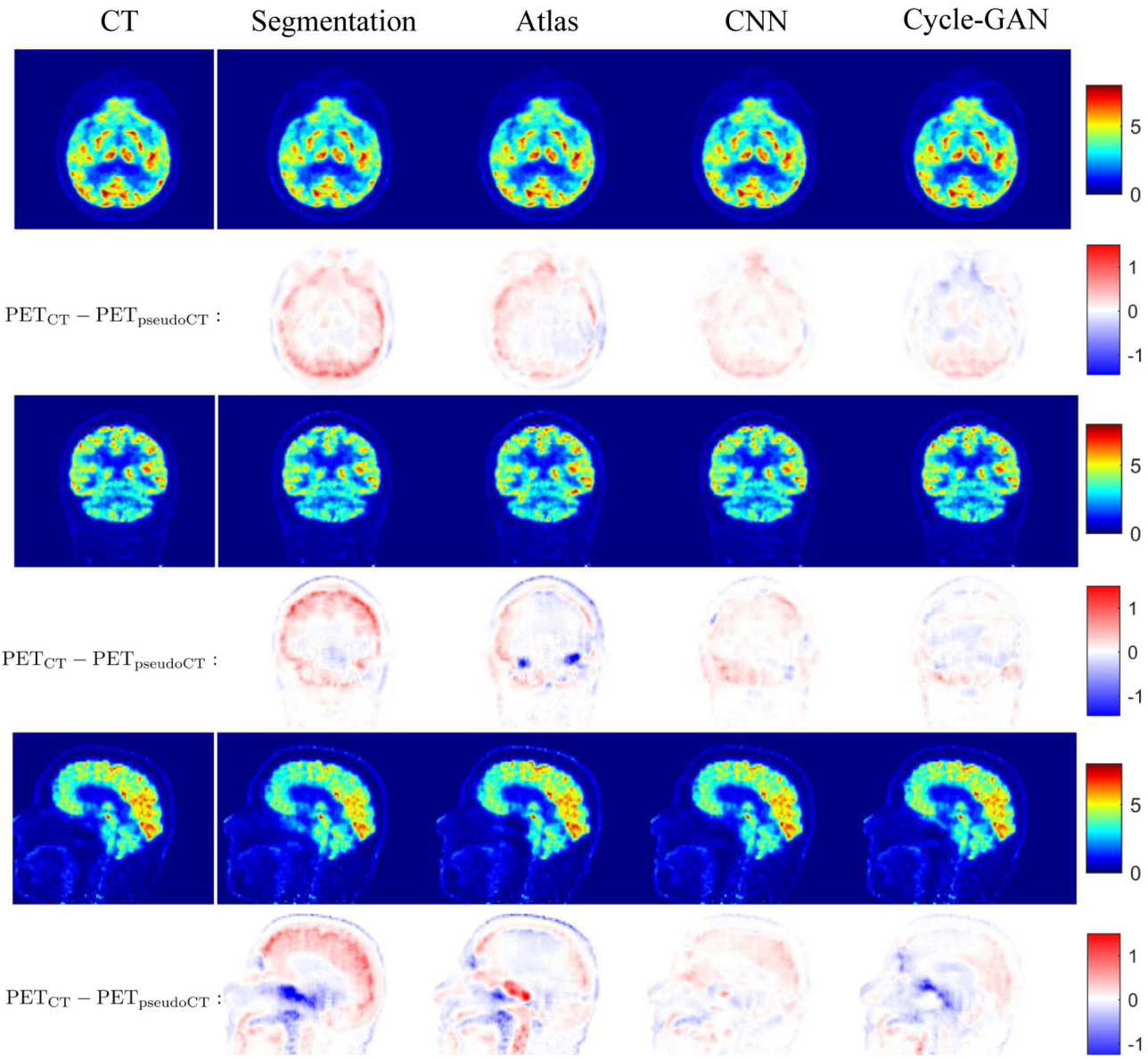

Fig. 4:

Three views of the SUV images reconstructed using different methods along with the corresponding SUV error images ($\mathrm{PET_{CT}} - \mathrm{PET_{pseudoCT}}$). The first column represents the SUV images generated by the ground-truth CT image. Starting from the second column, each column represents the SUV images and the corresponding SUV error images ($\mathrm{PET_{CT}} - \mathrm{PET_{pseudoCT}}$) using pseudo CT images generated by the Segmentation method, the Atlas method, the CNN method, and the Cycle-GAN method, respectively.

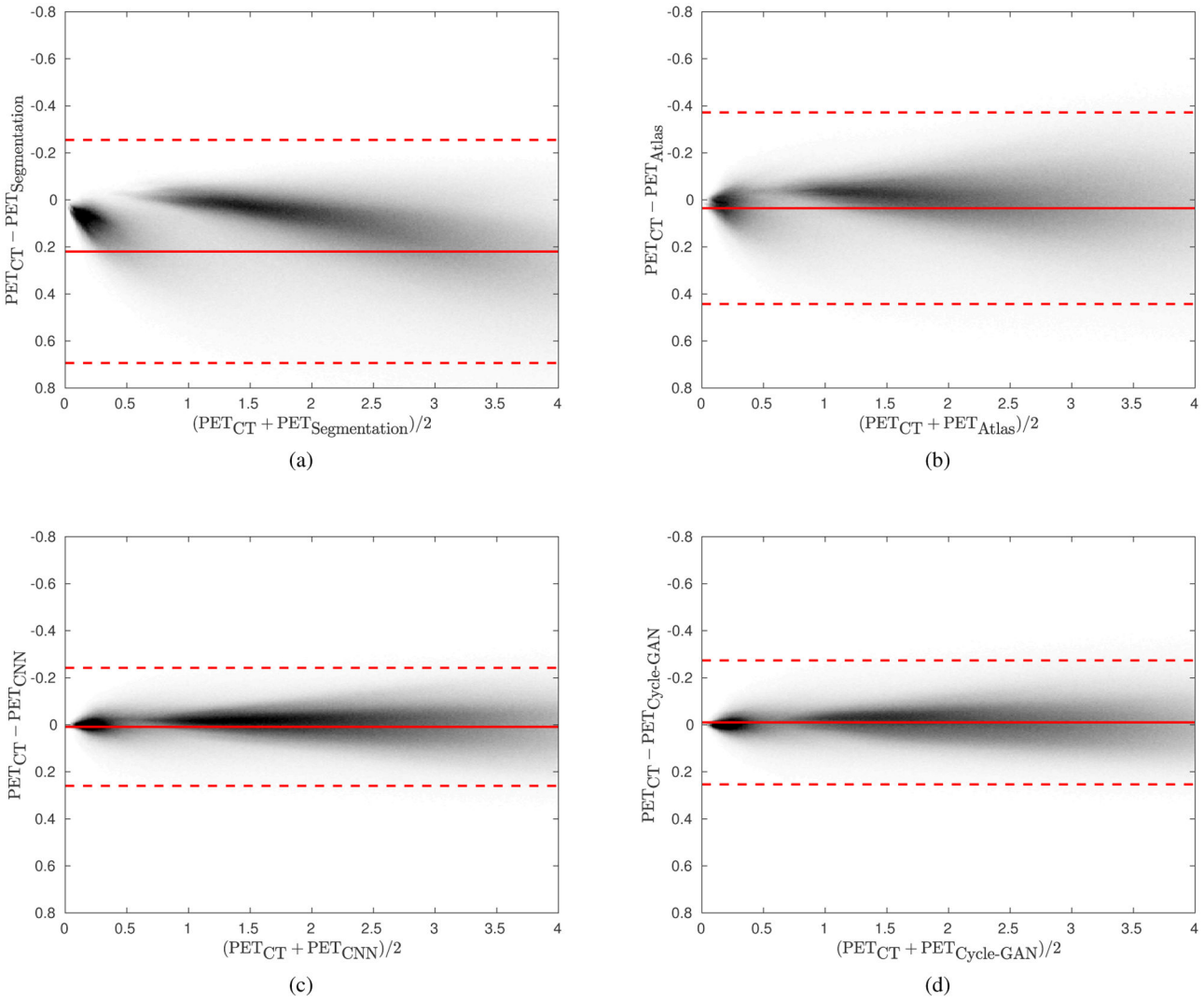

Fig. 5:

Bland-Altman plots for (a) Segmentation, (b) Atlas, (c) CNN, and (d) Cycle-GAN methods. The *x*-axis stands for the mean SUV value between the PET images reconstructed using the ground-truth CT and generated pseudo-CT images. The *y*-axis stands for the SUV difference between the PET images reconstructed using the ground-truth CT and generated pseudo-CT images.

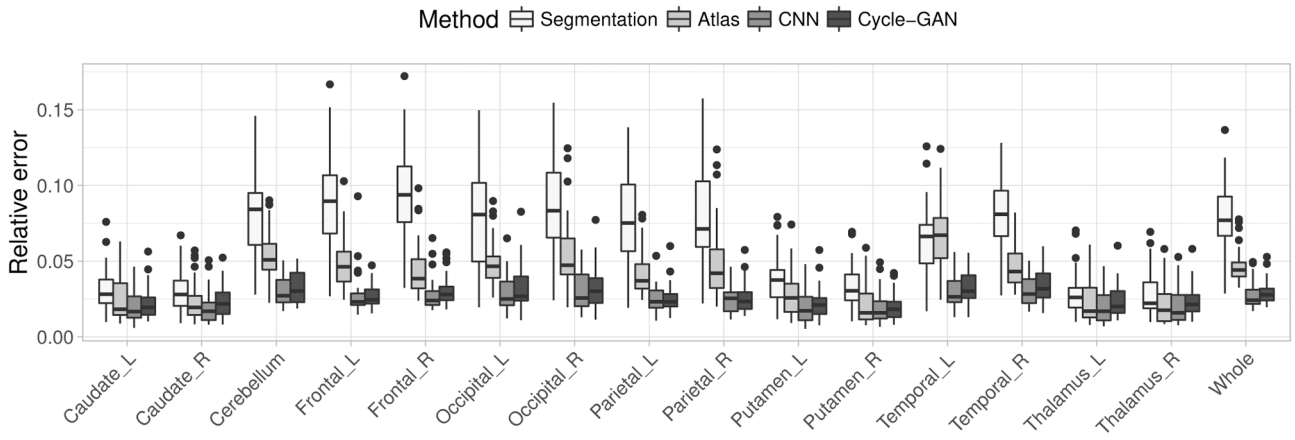

Fig. 6:

Global and regional relative errors for the Segmentation, Atlas, CNN and Cycle-GAN methods. The postfix of ‘L’ and ‘R’ of the regions stand for the left and right hemispheres, respectively.

TABLE I:

Comparisons of the generated pseudo CT images based on 32 datasets. The Dice index of bone regions was computed for the whole brain, regions above and below the eyes.

Methods	Relative validation loss	Dice of bone: whole	Dice of bone : above eye	Dice of bone : below eye
Segmentation	32.05 ± 5.88%	–	–	–
Atlas	23.10 ± 2.60%	0.52 ± 0.06	0.61 ± 0.07	0.29 ± 0.05
CNN	14.04 ± 1.85%	0.76 ± 0.05	0.82 ± 0.04	0.63 ± 0.07
Cycle-GAN	15.82 ± 2.36%	0.74 ± 0.05	0.81 ± 0.04	0.59 ± 0.07

IEEE Trans Radiat Plasma Med Sci. Author manuscript; available in PMC 2022 March 01.